

Two-dimensional charge order stabilized in clean polytype heterostructures

Suk Hyun Sung

University of Michigan-Ann Arbor <https://orcid.org/0000-0002-7491-1988>

Noah Schnitzer

Cornell University

Steve Novakov

University of Michigan <https://orcid.org/0000-0003-2467-4061>

Ismail El Baggari

Harvard University

Xiangpeng Luo

University of Michigan

Jiseok Gim

University of Michigan-Ann Arbor <https://orcid.org/0000-0001-7499-873X>

Nguyen Vu

University of Michigan-Ann Arbor

Zidong Li

University of Michigan-Ann Arbor <https://orcid.org/0000-0002-0984-9778>

Todd Brintlinger

Naval Research Laboratory <https://orcid.org/0000-0001-7959-4769>

Yu Liu

Key Laboratory of Materials Physics, Institute of Solid State Physics, Chinese Academy of Sciences, Hefei 230031, People's Republic of China

Wenjian Lu

Key Laboratory of Materials Physics, Institute of Solid State Physics, Chinese Academy of Sciences, Hefei 230031, People's Republic of China

Yuping Sun

Institute of Solid State Physics Chinese Academy of Sciences Hefei <https://orcid.org/0000-0003-2477-285X>

Parag Deotare

University of Michigan

Kai Sun

University of Michigan-Ann Arbor <https://orcid.org/0000-0001-9595-7646>

Liuyan Zhao

University of Michigan-Ann Arbor <https://orcid.org/0000-0001-9512-3537>

Lena Kourkoutis

Cornell University <https://orcid.org/0000-0002-1303-1362>

John Heron

University of Michigan–Ann Arbor

Robert Hovden (✉ hovden@umich.edu)

University of Michigan <https://orcid.org/0000-0002-3403-8803>

Article

Keywords: electron behavior, 2D charge density waves (CDWs)

Posted Date: February 24th, 2021

DOI: <https://doi.org/10.21203/rs.3.rs-253098/v1>

License:   This work is licensed under a Creative Commons Attribution 4.0 International License.

[Read Full License](#)

Version of Record: A version of this preprint was published at Nature Communications on January 20th, 2022. See the published version at <https://doi.org/10.1038/s41467-021-27947-5>.

Two-dimensional charge order stabilized in clean polytype heterostructures

Suk Hyun Sung¹, Noah Schnitzer^{2,3}, Steve Novakov⁴, Ismail El Baggari⁵, Xiangpeng Luo⁴, Jiseok Gim¹, Nguyen Vu¹, Zidong Li⁶, Todd Brintlinger⁷, Yu Liu⁸, Wenjian Lu⁸, Yuping Sun^{8,9}, Parag Deotare^{6,10}, Kai Sun⁴, Liuyan Zhao⁴, Lena F. Kourkoutis^{3,11}, John T. Heron^{1,10}, and Robert Hovden^{1,10,*}

¹Department of Materials Science and Engineering, University of Michigan, Ann Arbor, MI 48109. ²Department of Materials Science and Engineering, Cornell University, Ithaca, NY 14853. ³Kavli Institute at Cornell for Nanoscale Science, Ithaca, NY 14853. ⁴Department of Physics, University of Michigan, Ann Arbor, MI 48109. ⁵Department of Physics, Cornell University, Ithaca, NY 14853. ⁶Electrical and Computer Engineering Department, University of Michigan, Ann Arbor, MI 48109. ⁷Materials Science and Technology Division, U.S. Naval Research Laboratory, Washington, D.C. 20375. ⁸Key Laboratory of Materials Physics, Institute of Solid State Physics, Chinese Academy of Sciences, Hefei 230031, People's Republic of China. ⁹High Magnetic Field Laboratory, Chinese Academy of Sciences, Hefei 230031, People's Republic of China. ¹⁰Applied Physics Program, University of Michigan, Ann Arbor, MI 48109. ¹¹School of Applied and Engineering Physics, Cornell University, Ithaca, NY 14853. *e-mail: hovden@umich.edu

Strong evidence suggests that transformative correlated electron behavior may exist only in unrealized clean-limit 2D materials such as 1T-TaS₂. Unfortunately, experiment and theory suggest that extrinsic disorder in free standing 2D layers impedes correlation-driven quantum behavior. Here we demonstrate a new route to realizing fragile 2D quantum states through epitaxial polytype engineering of van der Waals materials. The isolation of truly 2D charge density waves (CDWs) between metallic layers stabilizes commensurate long-range order and lifts the coupling between neighboring CDW layers to restore mirror symmetries via interlayer CDW twinning. The twinned-commensurate charge density wave (tC-CDW) reported herein has a single metal–insulator phase transition at ~350 K as measured structurally and electronically. Fast in-situ transmission electron microscopy and scanned nanobeam diffraction map the formation of tC-CDWs. This work introduces epitaxial polytype engineering of van der Waals materials to access latent 2D ground states distinct from conventional 2D fabrication.

Introduction

Charge density wave (CDW) is an emergent periodic modulation of the electron density that permeates a crystal with strong electron-lattice coupling [1, 2]. TaS₂ and TaS_xSe_{2-x} host several CDWs that spontaneously break crystal symmetries, mediate metal–insulator transitions [3, 4], and compete with superconductivity [5–7]. These quantum states are promising candidates for novel devices [8–11], efficient ultrafast non-volatile switching [12, 13], and suggest elusive chiral superconductivity [14, 15]. Law & Lee recently called for pristine 2D CDW syntheses to access exotic spin-liquid states in 1T-TaS₂ [16]. Unfortunately, extrinsic and thermal disorder in free standing 2D layers degrades correlation-driven quantum behavior [17, 18] and clean-limit 2D charge density waves or superconductivity are near absent [19]. Room temperature access to spatially coherent charge density waves (e.g. commensurate states) and clean-limit 2D confinement could enable a paradigm shift toward device logic and quantum computing.

Here we show the critical temperature for spatially-coherent, commensurate charge density waves (C-CDW) in 1T-TaS₂ can be raised to well above room temperature (~150 K above the expected transition) by synthesizing clean interdigitated 2D polytypic heterostructures. This stabilizes a collective insulating ground state not expected to exist at room temperature. We show the formation of these spatially coherent states occurs when 2D CDWs are confined between metallic prismatic polytypes. Metallic layers screen impurity potentials to suppress the disordered nearly-commensurate (NC-CDW) phase. At the same time, interdigitation disables interlayer coupling between CDWs to ensure an unpaired electron in each 2D supercell. This raises the critical temperature of the C-CDW and forms out-of-plane twinned commensurate (tC) CDWs as revealed by scanned nanobeam electron

diffraction. These results demonstrate polytype engineering as a route to isolating 2D collective quantum states in a well-defined extrinsic environment with identical chemistry but distinct band structure.

Layered TaS₂ polytypes (Supp. Fig. S1) are archetypal hosts to anomalous electronic properties associated with the formation of CDWs. The Ta coordination to six chalcogens dramatically changes its behavior. Prismatic coordination (Pr) found in the stable 2H polytype is metallic, even below the CDW onset around 90 K, and becomes superconducting around 0.5 K (enhanced to 2.2 K when thinned [5]). Octahedral (Oc) coordination found in the metastable 1T polytype has inversion symmetry and exhibits three distinct CDW phases: commensurate (C), nearly-commensurate (NC), and incommensurate (IC). At room temperature, the conductive NC-CDW is generally accepted as a C-CDW with short range order [20–22] that permits electron transport along regions of discommensuration [23, 24]. Below ~200 K, the CDW wave vector locks into ~13.9° away from the reciprocal lattice vector (Γ –M) to become a C-CDW that achieves long-range order with a $\sqrt{13} \times \sqrt{13}$ supercell [1, 25]. This reduction of crystal symmetry gaps the Fermi-surface and the commensurate phase becomes Mott insulating [1, 26, 27]. Above 352 K, the CDW wave vector aligns along the reciprocal lattice vector and becomes the disordered IC-CDW phase.

Results

Twinned Commensurate Charge Density Waves

The tC-CDW phase reported herein has distinct out-of-plane charge order—illustrated in Figure 1a. 2D CDWs reside within Oc-layers sparsely interdigitated between metallic Pr-layers. Each

CDW is commensurate in one of two degenerate twin states, α -C (blue) or β -C (red) (Fig. 1b, c). The translational symmetry is described by in-plane CDW lattice vectors ($\lambda_{\alpha 1}, \lambda_{\alpha 2}$) and ($\lambda_{\beta 1}, \lambda_{\beta 2}$).

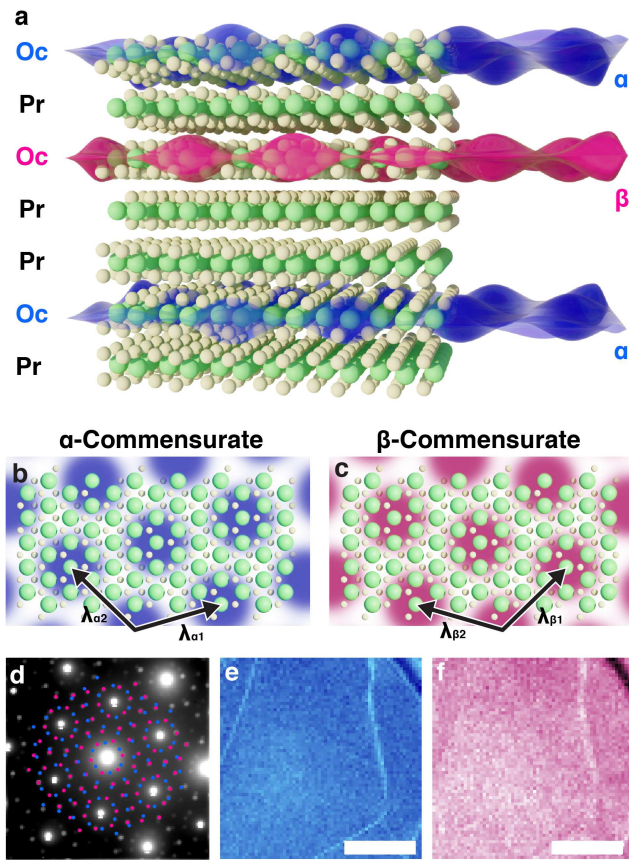


Fig. 1 | Twinned, commensurate CDW at room temperature in ultrathin TaS₂. a) Schematic illustration of room-temperature, out-of-plane twinned, commensurate CDW in 1T-TaS₂. Blue and red overlays represent CDW twins within octahedrally coordinated TaS₂. Metallic prismatic polytypes isolate octahedral layers to stabilize tC-CDWs. b, c) Twin superlattice structure illustrated for α and β C-CDW, respectively. d) Average diffraction pattern of twinned, C-CDW state over (870 nm)² field-of-view reveals two sets of superlattice peaks (marked with blue and red). e, f) Nanobeam diffraction imaging from each set of superlattice peaks maps the coexistence of both CDW twins—expected for twinning out-of-plane. Scale bar is 300 nm.

CDWs are a prototypical manifestation of electron-lattice coupling, in which both the electron density and lattice positions undergo periodic modulations to reduce crystal symmetry and lower the electronic energy [28]. The associated periodic lattice distortions (PLD) diffract incident swift electrons into low-intensity superlattice peaks between Bragg peaks [29, 30] (See also: Supplemental section SI2). Figure 1d shows the position averaged convergent beam electron diffraction pattern (0.55 mrad semi-convergence angle, 80 keV) of the tC-CDW phase at room temperature with α , β superlattice peaks annotated (blue, red). Regularly spaced superlattice peaks and bright first order superlattice peaks are characteristic of C-CDWs and match the tC-CDW peaks.

Both α and β CDW states were mapped over microns of area to reveal a uniform co-existence of both twins when viewed in projection out-of-plane (Fig. 1e, f). This is evidently different from recently reported in-plane twin CDWs created by femtosecond light pulses [31]. CDW structure was imaged using the diffracted inten-

sity of every α or β superlattice peak from a convergent electron beam (Fig. 1e, f) rastered across the specimen—an emerging technique often called 4D-STEM (See Methods) [32–34]. In this way, the local CDW structure was measured at ~ 4.6 nm resolution and across > 1 μm fields of view. Previous approaches to mapping CDWs entailed sparse measurement from a handful of diffraction patterns [31], small-area tracking of atomic displacements [35], or traditional dark-field TEM techniques that result in low resolution and debilitating signal-to-noise ratios [1, 36].

Clean-Limit Polytype Heterostructures

Thermal treatment reproducibly forms the tC-CDW phase—a process summarized by the in-situ selected area electron diffraction (SAED) in Figure 2a. Initially, an exfoliated flake of 1T-TaS₂ hosts NC-CDWs (Fig. 2a, left) at room temperature with diffuse first-order superlattice peaks (cyan circles) and sharp second order superlattice peaks (cyan triangle). 1T-TaS₂ is heated past the reversible phase transition ($T_{\text{NC-IC}} \approx 352$ K) into the disordered IC-CDW state, which has characteristic azimuthally diffuse superlattice spots (Fig. 2a, right). Heating continues up to temperatures (~ 720 K) above the polytype transition ($T_{\text{Oc-Pr}} \approx 600$ K [37]) where it remains for several minutes (see Methods). Upon cooling, the system does not return to the expected NC-CDW but instead enters a tC-CDW state with sharp, commensurate first and second order superlattice peaks duplicated with mirror symmetry (α , β) (Fig. 2a, bottom). The tC-CDW phase is stable and observable after months of dry storage (RH ~ 10 %) at room temperature. Synthesis was replicated ex-situ in both high-vacuum ($< 10^{-7}$ Torr) and inert argon purged gloveboxes, but amorphized in ambient air. The tC-CDW was equivalently synthesized for both TaS₂ and TaS_xSe_{2-x}.

Heating above the polytype transition temperature ($T_{\text{Oc-Pr}}$) provokes layer-by-layer transitions from Oc to Pr polytypes instead of a rapid bulk transformation. Figure 2b–e shows in-situ TEM using high-frame-rate (25 fps) microscopy taken at ~ 710 K. Each colored overlay highlights the growth and formation of a new prismatic polytype domain (raw data in Supp. Fig. S4). Arrows indicate movement of Oc/Pr coordination boundary with a fast-transition up to $\sim 10^2$ nm/s along $\langle 10\bar{1}0 \rangle$ crystal directions and a slow-transition at ~ 10 nm/s along $\langle 11\bar{2}0 \rangle$ (Fig. 2g). Video of the transformation is striking (Supplemental Video). Domains nucleate and boundaries progress independently between layers as illustrated in Figure 2b–f. Cooling the sample mid-transition produces a sparsely interdigitated polytypic heterostructure.

Atomic resolution cross-section images of pristine and heat-treated samples (Fig. 2h and i, respectively) measured by high-angle annular dark-field (HAADF)-STEM reveal the interdigitated polytypic heterostructure. Interdigitation isolates monolayers of octahedral (Oc) coordination that host 2D-CDWs in a clean, defect-free environment of prismatic (Pr) metallic layers.

The metallic ‘Pr’ layers are hypothesized to screen out-of-plane interactions and impurity potentials to stabilize low-temperature commensurate CDWs at room temperature. As a result, the NC-CDW state no longer exists and a long-range ordered tC-CDW emerges as a stable phase up to ~ 350 K. This result is radically different from previous reports where free standing ultra-thin 1T-TaS₂

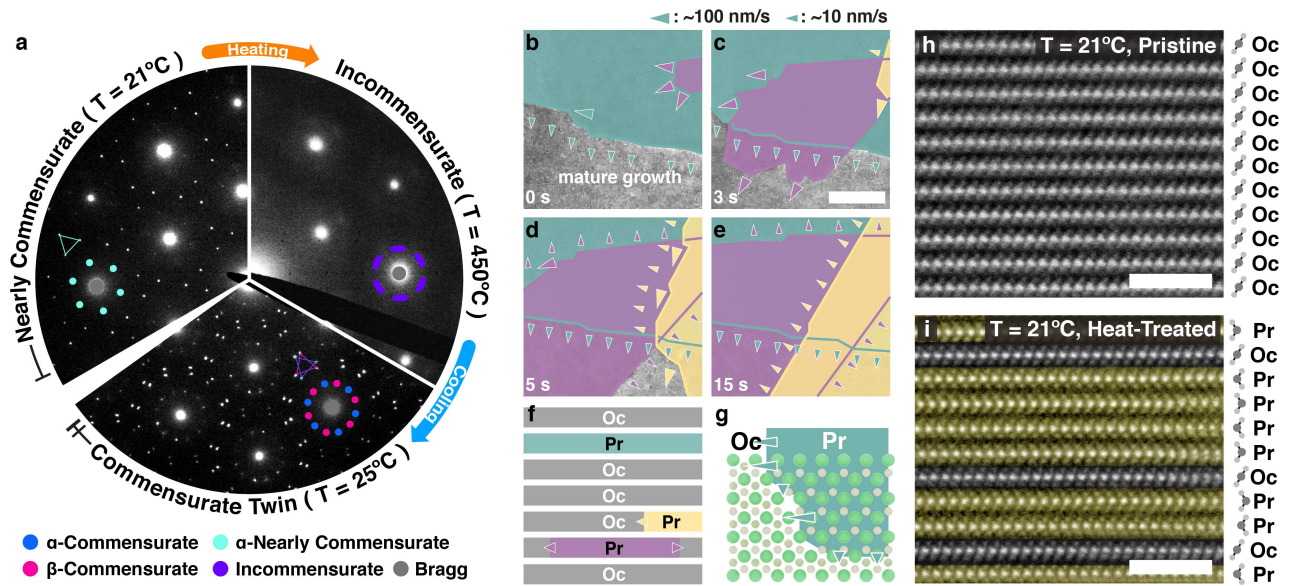


Fig.2 | Polytype isolation forms 2D CDW layers. a) Pristine 1T-TaS₂ at room temperature hosts NC-CDW (left). Upon heating the NC phase gives way to IC-CDW (right) at $\sim 80^\circ\text{C}$; the transition is normally reversible. Strikingly, heating above $\sim 350^\circ\text{C}$ then cooling stabilizes tC-CDW (bottom) b–e) In-situ TEM reveals layer-by-layer octahedral to prismatic polytypic transformations during heat treatment. Multiple polytypic domains (denoted green, purple, and yellow) nucleate and grow simultaneously without interaction (See Supplemental Video). Scale bar is 350 nm. f) Schematic cross-section of TaS₂ during layer-by-layer polytypic transition. g) Fast and slow transitions occur along $\langle 10\bar{1}0 \rangle$ and $\langle 11\bar{2}0 \rangle$ directions respectively. h–i) Atomic resolution cross-sectional HAADF-STEM of h) pristine and i) heat-treated TaS_xSe_{2-x} confirms polytypic transformation. After treatment, prismatic (Pr) layers encapsulate monolayers of octahedral (Oc) layers. Scale bar is 2 nm. A selenium doped sample was imaged to enhance chalcogen visibility.

degrades long-range order [38] and broadens the NC-CDW phase by lowering T_{CDW} [13, 18, 39]. However, our observation of 2D commensurate CDWs agrees with a theoretical prediction that commensurate CDWs are more stable in clean monolayer [40].

Understanding the role of disorder requires decoupling intrinsic quantum behavior from extrinsic influences at the surfaces, especially in low dimensions where long-range order becomes more fragile and vulnerable to impurities [17, 41, 42]. When the disorder strength reaches a certain threshold, the long-range C-CDW phase gives its way to a disordered phase [17]. Here, each 2D 1T-TaS₂ CDW is in its native chemical, epitaxial, and unstrained environment. Impurity potentials that pin CDWs [43] and break spatial coherence are mitigated by adjacent metallic Pr-layers. For C-CDWs (in 2D and above) in the presence of sufficiently weak disorder, the charge order remains stable [42]. Additionally, isolating monolayers of 1T-TaS₂ ensures an odd number of electrons per unit cell and elongates the Fermi surface out-of-plane—both expected to reduce the electronic energy.

Isolation of 2D Charge Density Waves

In the tC-CDW, metallic Pr-layers decouple interlayer CDW interactions to create isolated 2D CDWs with twin degeneracy. Using a phenomenological Landau model we illustrate a kinetic pathway for accessing the tC-CDW. Here, local orientation of the CDW wave vector, θ , is an apt order parameter for describing symmetry breaking of $C \rightleftharpoons IC$ transitions (See Methods). A Landau free energy expansion of this order parameter combined with an XY interaction of the CDW wave vector (see Methods) reproduces diffraction patterns for IC-CDW and α/β C-CDW. In diffraction, the superlattice peak location and shape encodes the distribution of the CDW order parameter. Simulated diffraction

patterns at high temperatures feature first-order superlattice peaks azimuthally broadened by CDW disorder and centered along the reciprocal lattice (Γ -M) direction (Fig. 3b). At low temperature, the superlattice peaks are sharpened by long-range CDW order and located at $+13.9^\circ$ or -13.9° away from Γ -M (Fig. 3a,c). Figure 3d shows distribution of θ at high (gray) and low (blue, red) temperatures.

When cooled, the system chooses α or β with equal probability. For pristine 1T-TaS₂, CDWs couple between layers, twin degeneracy is broken, and no twinning occurs [44]. However, in the absence of interlayer interaction or extrinsic perturbation, each 2D CDW layer quenches randomly into either α or β C-CDW (Fig. 3g) from the high-temperature IC-CDW phase (Fig. 3f)—forming the out-of-plane twinned tC-CDW phase. From our model, out-of-plane twinning occurs for modest cooling rates but we note fast quenching predicts in-plane twinning (Supp. Fig. S7) similar to reported ultrafast optical excitations [31].

Optical and Electrical Characteristics of tC-CDW

Rotational-anisotropy second-harmonic generation (RA-SHG) revealed restoration of twin degeneracy in heat-treated samples. The RA-SHG of pristine sample (Fig. 4b) exhibits a hallmark of the RA-SHG pattern rotated away from the lattice vectors; breaking mirror symmetry due to formation of a single-domain NC-CDW. In contrast, the heat-treated sample's RA-SHG pattern (Fig. 4c) is mirror-symmetric to the crystalline directions and much stronger. Together, this is a strong evidence of equally weighted degenerate α and β states (i.e., tC-CDW) and the emergence of Pr-layers that are mirror symmetric and non-centrosymmetric.

Electronic measurement of the polytypic heterostructure with interdigitated CDWs reveals a direct $tC \rightleftharpoons IC$ transition at 350 K

and removal of the disordered NC-CDW phase. Figure 4a shows in-plane resistance vs. temperature measurements of pristine 1T (pink) and heat-treated polytypic heterostructure (blue) are drastically different. The heterostructure features only one metal–insulator transition at 350 K, whereas pristine 1T-TaS₂ exhibits two transitions at ~200 K (C \rightleftharpoons NC) and 350 K (NC \rightleftharpoons IC). Resistance jumps are a signature of emergent CDW order. At low temperature the metallic Pr-layers dominate in-plane conduction since the resistance is expected to monotonically decrease as observed in bulk material [45]. This hinders the quantification of resistance in individual Oc-layers, however the critical temperatures remain clearly visible.

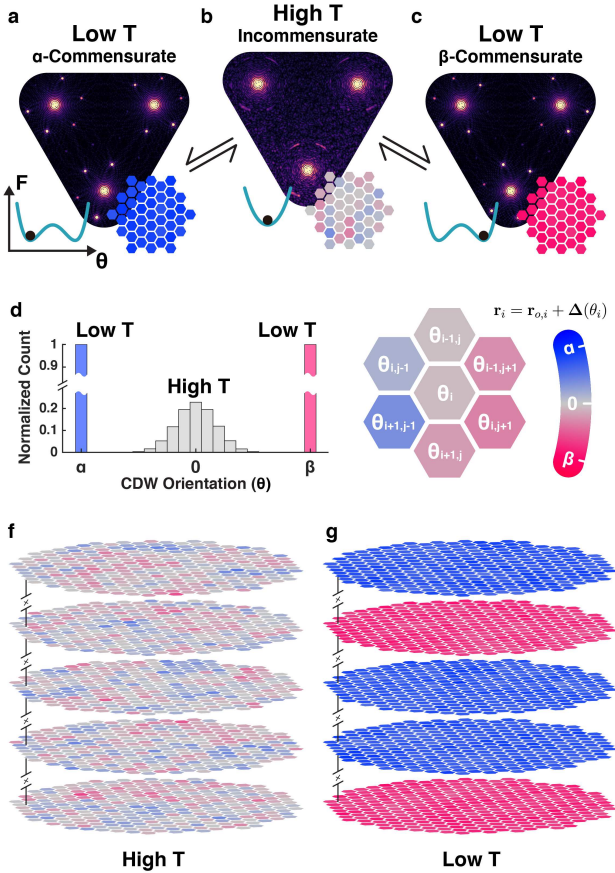


Fig.3 | Phenomenological Landau model illustrates formation of commensurate CDWs with out-of-plane twin degeneracy. a–c) The CDW wave-vector direction θ defines an order parameter with degenerate commensurate twins when cooled from IC-CDW phase. Simulated far-field diffraction patterns for a) α -C, b) IC and c) β -C. The free energy (F) landscape (Inset-left) governs the mean θ and the real-space distribution (Inset-right). d) Histogram of θ shows zero-centered, wide distribution at high temperature. At low temperature, the distribution is narrow and centered at $\pm 13.9^\circ$ for either twin. e) Six nearest-neighbor interactions drives long-range order of the CDW. f) At high temperature θ is mean centered and disordered, however, g) at low-temperature each 2D layer converges into either α or β randomly when layers are decoupled.

Repeated in-situ heating–cooling cycles reveal the tC \rightleftharpoons IC transition is reversible and the NC-CDW phase is removed. Electronic measurements (Fig. 4a) match structure measurements from in-situ SAED (Fig. 2a) and confirm the insulating commensurate charge order of the tC-CDW phase. The interdigitated polytype herein stabilizes coherent electronic states well above (~150 K)

the normal critical temperature, and disordered NC-CDW phase is structurally and electronically removed.

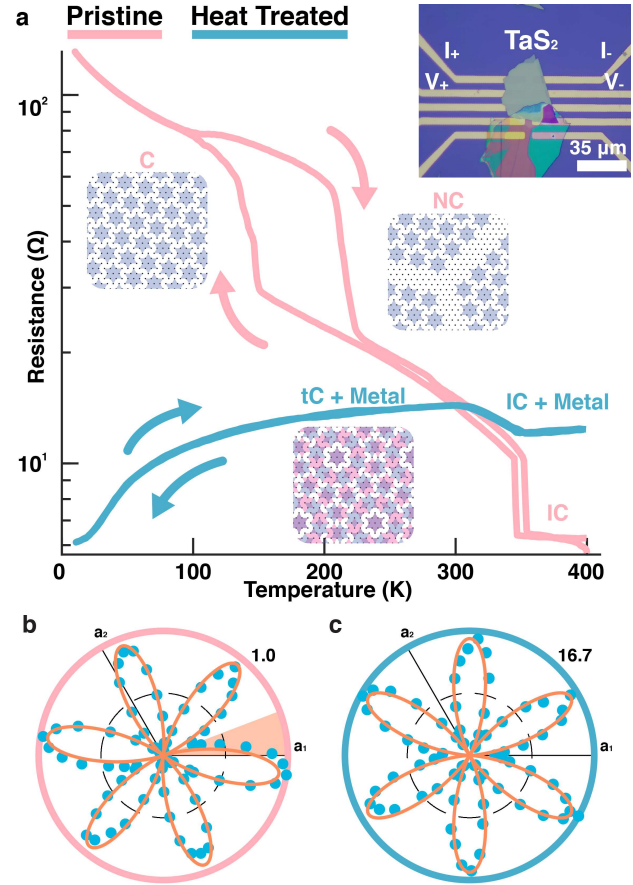


Fig.4 | Electronic transport of tC-CDW phase transition and reversibility. a) 4-point in-plane resistance measurement as function of temperature for pristine bulk (pink) and heat-treated (blue) TaS₂. Pristine samples show two jumps in resistance for C \rightleftharpoons NC and NC \rightleftharpoons IC, whereas the heat treated polytypic heterostructures only feature a single, reversible tC \rightleftharpoons IC transition at ~350 K corresponding to the enhanced critical temperature for CDW commensuration and disappearance of the NC-CDW. Metallic Pr-layers dominate the overall trend of the resistance measurement, however, the single jump above room-temperature is a distinct feature of the tC-CDW. Inset) Optical image of the nanofabricated device. b) The RA-SHG pattern for pristine 1T samples display a mismatch between the nominal mirror direction and the crystalline direction, indicating the CDW breaks mirror symmetry. c) After heat treatment, the RA-SHG pattern is symmetric with respect to the crystal, implying equal weights between the α and β states. The SHG intensity also increases with mirror symmetric Pr-layers present.

Discussion

In summary, latent CDWs with long-range order were stabilized at room-temperature by reducing their dimension to 2D in a clean-limit using engineered interdigitated polytypes of TaS₂. The metallic layers isolate each 2D CDW to restore twin degeneracy giving rise to an out-of-plane twinned commensurate CDW phase. 4D-STEM proved invaluable for mapping CDW domains across large fields-of-view (~1 μ m) to confirm twin structure while atomic resolution HAADF-STEM revealed the 2D CDW layers within a metallic phase. Both structural and electronic investigations show the disordered NC-CDW phase disappears when a 2D CDW in a chemically and epitaxially native environment. The stabilization of ordered electronic phases with 2D polytype

engineering has significant implications for new routes to access fragile, exotic correlated electron states.

Methods

Electron Microscopy

Mapping CDW structure required a pixel array detector to collect a convergent beam electron diffraction pattern at every beam position across large fields-of-view (i.e. 4D-STEM). In-situ 4D-STEM was performed on FEI Titan Themis 300 (80 keV, 0.55 mrad convergence semi-angle) with electron microscope pixel array detector (EMPAD) and DENS Wildfire heating holder. For 4D-STEM, a convergent beam electron diffraction (CBED) pattern was recorded at each beam position using the EMPAD detector. EMPAD's high dynamic range (1,000,000:1) and single electron sensitivity [32] allows simultaneous recording of intense Bragg beams alongside weak superlattice reflections. Virtual satellite dark field images were formed by integrating intensities from all satellite peaks at each scan position.

In-situ TEM revealed layer-by-layer polytypic transition. The polytype difference is indiscernible in low-magnification with HAADF-STEM, as two polytypes have equal density. However, the change in bond coordination at polytype boundaries provide visible coherent contrast in TEM. The in-situ movie and SAED patterns were taken with JEOL 2010F (operated at 200 keV) with Gatan Heater Holder and Gatan OneView Camera. Both sample for 4D-STEM and TEM were prepared by exfoliating bulk 1T-TaS₂ crystal on to PDMS gel stamp, then transferring on to a TEM grid.

Cross-sectional HAADF-STEM images were taken on JEOL 3100R05 (300 keV, 22 mrad) with samples prepared on FEI Nova Nanolab DualBeam FIB/SEM.

Synthesis of 1T-TaS_xSe_{2-x} crystal

High-quality single crystals of 1T-TaS_xSe_{2-x} ($0 \leq x \leq 2$) were grown by the chemical vapor transport method with iodine as a transport agent. Stoichiometric amounts of the raw materials, high-purity elements Ta, S and Se, were mixed and heated at 900 °C for 4 days in an evacuated quartz tube. Then the obtained TaS_xSe_{2-x} powders and iodine (density: 5 mg/cm³) were sealed in another longer quartz tube, and heated for 10 days in a two-zone furnace, where the temperature of source zone and growth zone was fixed at 950 °C and 850 °C, respectively. A shiny mirror-like sample surface was obtained, confirming their high quality.

Thermal Synthesis of tC-CDW in TaS₂

Interdigitated 2D TaS₂ polytypes were synthesized by heating 1T-TaS₂ to 720 K in high vacuum ($< 10^{-7}$ Torr) or in an argon purged glovebox. 1T-TaS₂ was held at 720 K for ~10 minutes, then brought down to room temperature. Once the interdigitated polytype is fully established, the tC-CDW becomes stable electronic state up to 350 K. Synthesis is sensitive the duration held at high temperature. Notably, if the sample is not held long enough at elevated temperature, NC-C twin phase was reached (See Supplemental Figure S8), due to sparse distribution of Pr-layers encapsulating multilayer 1T-TaS₂. Both slow (~1 K/sec) and fast (~10 K/sec) cooling rate produced out-of-plane twinning.

Device Fabrication and Electronic Measurement

Sample lithography was done with a standard SPR-220 based process using a Heidelberg μ PG 501 maskless exposure tool to directly expose samples. The bottom contact pattern was exposed on a silicon wafer with 500 nm SiO₂. To limit damage and bending to the TaS₂ flakes, the bottom contact liftoff pattern was first ion beam etched with Ar to a 60 nm depth. The trenches were then back-filled with 10 nm Ti and 50 nm Au, deposited in an e-beam evaporator at 3 Å/s, and excess metal was lifted-off using acetone/isopropanol sonication of the wafer. The resulting contacts are level to the wafer surface to within 5 nm, as confirmed by AFM. Before flake exfoliation, the bottom contacts were gently polished using 100 nm micropolishing film to remove liftoff fingers, which can extend up to 30 nm above the wafer surface. Each bottom contact pattern includes six 5 μ m striplines spaced 5 μ m apart, and eight radial pads of approximately 500 \times 500 μ m for top contact fan-out.

Resistance vs. temperature measurements were performed in a Quantum Design Dynacool PPMS using a standard sample puck and an external Keithley 2400 series source meter. The sample was adhered to the puck backplane with silver paint, and contacts were wire bonded to the puck channel pads using 50 μ m Au wire. To ensure sample thermalization, a baffle rod with an Au-coated sealing disk hovering <1 cm above the sample was inserted into the PPMS bore, and the heating and cooling rate was restricted to <2 K/min. Depending on sample characteristics, between 20–200 μ A current was sourced for four wire measurements. The current/voltage limits were chosen to keep electric fields below 10 kV/cm to avoid sample breakdown, as well as to keep current densities below 10⁵ A/cm² and prevent localized heating at low temperatures. Due to sample variability, such as inter-layer CDW phase differences and mechanical variability such as tears or holes in flakes, these limits are approximate in general scanning. In cases where samples transformed into bulk prismatic phase, they are better observed.

Modelling C \rightleftharpoons IC transition

We describe the free energy landscape using Landau expansion:

$$f_i(T) = a_2(T - T_c)\theta_i^2 + a_4\theta_i^4 + \sum_{nn}^6 \cos(\theta_{nn} - \theta_i)^2 \quad (1)$$

with f , T , T_c , a , θ denotes local free energy, temperature, transition temperature, Landau energy coefficient, and local CDW orientation respectively. The last term is an XY nearest-neighbor interaction that enforces smoothness; in the continuum limit, it converges to $|\nabla\theta|^2$. We chose 6 nearest-neighbors to accommodate the crystal symmetry (Fig. 3c). The simulation was done on hexagonal grid with 65536 sites and periodic boundary condition.

The distribution of θ was calculated using Markov Chain Monte Carlo simulation with Metropolis-Hasting algorithm. Initially, a random distribution θ was generated. At each iteration, 40% of sites were randomly selected, then randomly generated θ were accepted or rejected based on Boltzmann statistics: $\exp[-\Delta f/k_B T]$. The effect of cooling was simulated in simulated annealing manner where initial T was set to $2T_c$ then reduced by $0.2T_c$ every 10^{10} iterations.

To simulate far-field diffraction from simulated θ , each lattice position (\mathbf{r}_i) was distorted with three longitudinal modulation waves with wave vector $\mathbf{q}_{i,1}, \mathbf{q}_{i,2}, \mathbf{q}_{i,3}$ along $\theta_i, \theta_i + 120^\circ, \theta_i + 240^\circ$: $\mathbf{r}'_i = \mathbf{r}_i + \sum_{n=1,2,3} \mathbf{A}_n \sin(\mathbf{q}_{i,n} \cdot \mathbf{r}_i)$. Far-field diffraction ($I(\mathbf{k})$) was calculated by taking modulus squared of plane waves from each lattice sites: $I(\mathbf{k}) = |\sum_i \exp[i\mathbf{k} \cdot \mathbf{r}'_i]|^2$.

RA-SHG Measurements

The RA-SHG measurements were performed with the beam at normal incidence. The reflected SHG intensity is recorded as a function of the azimuthal angle between the incident electric polarization and the in-plane crystalline a -axis, with the reflected electric polarization being parallel to the incident one. In this experiment, the incident ultrafast light source was of 800 nm wavelength, 50 fs pulse duration and 200 kHz repetition rate, and was focused with a 5 μm diameter spot on the sample with a fluence of $\sim 0.2 \text{ mJ/cm}^2$. The intensity of the reflected SHG was measured with a single photon counting detector. SHG measurements was performed on $\text{Ta}_x\text{Se}_{2-x}$ sample, which has same point group symmetries with TaS_2 both before and after heat treatment.

Absorption Measurements

Home-build microscopic system with tungsten halogen source (Ocean Optics HL-2000-LL0) was used for absorption measurement. The transmitted signal was directed to Princeton Instruments IsoPlane-320 spectrometer, dispersed by 1200 grooves per mm diffraction grating, and detected by PIXIS: 400BR CCD camera.

References

- Wilson, J., Di Salvo, F. & Mahajan, S. Charge-density waves and superlattices in the metallic layered transition metal dichalcogenides. *Adv. Phys.* **24**, 117–201 (2 1975).
- Chan, S.-K. & Heine, V. Spin density wave and soft phonon mode from nesting Fermi surfaces. *J. Phys. F: Met. Phys.* **3**, 795 (4 1973).
- Boswell, F. W. & Prodan, A. Charge-density-waves of variable incommensurability in the system $\text{TaTe}_4 - \text{NbTe}_4$. *Mater. Res. Bull.* **19**, 93–97. ISSN: 0025-5408 (1984).
- Hellmann, S. *et al.* Time-domain classification of charge-density-wave insulators. *Nat. Commun.* **3**, 1069 (2012).
- Navarro-Moratalla, E. *et al.* Enhanced superconductivity in atomically thin TaS_2 . *Nat. Commun.* **7**, 11043 (1 Mar. 2016).
- Frindt, R. F. Superconductivity in Ultrathin NbSe_2 Layers. *Phys. Rev. Lett.* **28**, 299–301 (5 Jan. 1972).
- Joe, Y. I. *et al.* Emergence of charge density wave domain walls above the superconducting dome in 1T-TiSe_2 . *Nat. Phys.* **10**, 421–425 (2014).
- Basov, D. N., Averitt, R. D. & Hsieh, D. Towards properties on demand in quantum materials. *Nat. Mater.* **16**, 1077–1088. ISSN: 1476-1122 (2017).
- Tokura, Y., Kawasaki, M. & Nagaosa, N. Emergent functions of quantum materials. *Nat. Phys.* **13**, 1056–1068. ISSN: 1745-2473 (2017).
- Hollander, M. J. *et al.* Electrically Driven Reversible Insulator–Metal Phase Transition in 1T-TaS_2 . *Nano Lett.* **15**, 1861–1866. ISSN: 1530-6984 (2015).
- Liu, G. *et al.* A charge-density-wave oscillator based on an integrated tantalum disulfide–boron nitride–graphene device operating at room temperature. *Nat. Nanotechnol.* **11**, 845–850. ISSN: 1748-3387 (2016).
- Vaskivskiy, I. *et al.* Fast electronic resistance switching involving hidden charge density wave states. *Nat. Commun.* **7**, 11442 (2016).
- Tsen, A. W. *et al.* Structure and control of charge density waves in two-dimensional 1T-TaS_2 . *Proc. Natl. Acad. Sci.* **112**, 15054–15059 (49 2015).
- Ribak, A. *et al.* Chiral superconductivity in the alternate stacking compound 4Hb-TaS_2 . *Sci. Adv.* **6**, eaax9480 (2020).
- Ganesh, R., Baskaran, G., van den Brink, J. & Efremov, D. V. Theoretical Prediction of a Time-Reversal Broken Chiral Superconducting Phase Driven by Electronic Correlations in a Single TiSe_2 Layer. *Phys. Rev. Lett.* **113**, 177001 (17 Oct. 2014).
- Law, K. & Lee, P. 1T-TaS_2 as a quantum spin liquid. *Proc. Natl. Acad. Sci.* **114**, 6996–7000 (2017).
- Nie, L., Tarjus, G. & Kivelson, S. A. Quenched disorder and vestigial nematicity in the pseudogap regime of the cuprates. *Proc. Natl. Acad. Sci.* **111**, 7980–7985. ISSN: 0027-8424 (2014).
- Yu, Y. *et al.* Gate-tunable phase transitions in thin flakes of 1T-TaS_2 . *Nat. Nanotechnol.* **10**, 270–276 (2015).
- Devarakonda, A. *et al.* Clean 2D superconductivity in a bulk van der Waals superlattice. *Science* **370**, 231–236 (6513 2020).
- Wu, X. L. & Lieber, C. M. Hexagonal Domain-Like Charge Density Wave Phase of TaS_2 Determined by Scanning Tunneling Microscopy. *Science* **243**, 1703–1705 (4899 1989).
- Vogelgesang, S. *et al.* Phase ordering of charge density waves traced by ultrafast low-energy electron diffraction. *Nat. Phys.* **14**, 184–190 (2017).
- Hovden, R. *et al.* Atomic lattice disorder in charge-density-wave phases of exfoliated dichalcogenides (1T-TaS_2). *Proc. Natl. Acad. Sci.* **113**, 11420–11424 (41 2016).
- Cho, D. *et al.* Nanoscale manipulation of the Mott insulating state coupled to charge order in 1T-TaS_2 . *Nat. Commun.* **7**, 10453 (2016).
- Sipos, B. *et al.* From Mott state to superconductivity in 1T-TaS_2 . *Nat. Mater.* **7**, 960–965 (12 2008).
- Ishiguro, T. & Sato, H. Electron microscopy of phase transformations in 1T-TaS_2 . *Phys. Rev. B* **44**, 2046–2060 (5 1991).
- Johannes, M. D. & Mazin, I. I. Fermi surface nesting and the origin of charge density waves in metals. *Phys. Rev. B* **77**, 165135 (16 Apr. 2008).
- Rosnagel, K. On the origin of charge-density waves in select layered transition-metal dichalcogenides. *J. Phys.: Condens. Matter.* **23**, 213001 (2011).
- McMillan, W. L. Landau theory of charge-density waves in transition-metal dichalcogenides. *Phys. Rev. B* **12**, 1187–1196 (4 Aug. 1975).
- Overhauser, A. W. Observability of Charge-Density Waves by Neutron Diffraction. *Phys. Rev. B* **3**, 3173–3182 (10 May 1971).
- El Baggari, I. *et al.* Nature and evolution of incommensurate charge order in manganites visualized with cryogenic scanning transmission electron microscopy. *Proc. Natl. Acad. Sci.* **115**, 1445–1450 (7 2018).
- Zong, A. *et al.* Ultrafast manipulation of mirror domain walls in a charge density wave. *Sci. Adv.* **4**, eaau5501 (10 2018).
- Tate, M. W. *et al.* High Dynamic Range Pixel Array Detector for Scanning Transmission Electron Microscopy. *Microsc. Microanal.* **22**, 237–249 (2016).
- Panova, O. *et al.* Diffraction imaging of nanocrystalline structures in organic semiconductor molecular thin films. *Nat. Mater.* **18**, 860–865 (2019).
- Qiao, Q. *et al.* Anisotropic charge density wave in layered 1T-TiSe_2 . *Phys. Rev. Mat.* **1**, 054002 (2017).
- Savitzky, B. H. *et al.* Bending and breaking of stripes in a charge ordered manganite. *Nat. Commun.* **8**, 1883 (1 Dec. 2017).
- Chen, C. H., Gibson, J. M. & Fleming, R. M. Microstructure in the incommensurate and the commensurate charge-density-wave states of 2H-TaSe_2 : A direct observation by electron microscopy. *Phys. Rev. B* **26**, 184–205 (1 July 1982).
- Givens, F. L. & Fredericks, G. E. Thermal Expansion of NbSe_2 and TaS_2 . *J. Phys. Chem. Solids* **38**, 1363–1365 (12 1977).
- Sakabe, D., Liu, Z., Suenaga, K., Nakatsugawa, K. & Tanda, S. Direct observation of mono-layer, bi-layer, and tri-layer charge density waves in 1T-TaS_2 by transmission electron microscopy without a substrate. *npj Quantum Mater.* **2**, 22 (1 2017).
- Yoshida, M. *et al.* Controlling charge-density-wave states in nano-thick crystals of 1T-TaS_2 . *Sci. Rep.* **4**, 7302 (1 Dec. 2014).
- Darancet, P., Millis, A. J. & Marianetti, C. A. Three-dimensional metallic and two-dimensional insulating behavior in octahedral tantalum dichalcogenides. *Phys. Rev. B* **90**, 045134 (4 July 2014).
- Imry, Y. & Ma, S.-k. Random-Field Instability of the Ordered State of Continuous Symmetry. *Phys. Rev. Lett.* **35**, 1399–1401. ISSN: 0031-9007 (1975).
- Cardy, J. *Scaling and renormalization in statistical physics* (Cambridge university press, 1996).

43. Rice, T. M., Whitehouse, S. & Littlewood, P. Impurity pinning of discommensurations in charge-density waves. *Phys. Rev. B*, **24**, 2751–2759 (1981).
44. McMillan, W. L. Theory of discommensurations and the commensurate-incommensurate charge-density-wave phase transition. *Phys. Rev. B* **14**, 1496–1502. ISSN: 1098-0121 (1976).
45. Thompson, A. H., Gamble, F. R. & Koehler, R. F. Effects of Intercalation on Electron Transport in Tantalum Disulfide. *Phys. Rev. B* **5**, 2811–2816 (8 Apr. 1972).

Acknowledgements

S.H.S. acknowledges the financial support of the W.M. Keck Foundation. L.Z. acknowledges support by the NSF CAREER Grant No. DMR-1749774. Experiments were conducted using the Michigan Center for Materials Characterization (MC2) with assistance from Haiping Sun and Bobby Kerns and the Platform for the Accelerated Realization, Analysis, and Discovery of Interface Materials (PARADIM) supported by the National Science Foundation under Cooperative Agreement No. DMR-1539918. This work was performed in part at the University of Michigan Lurie Nanofabrication Facility with assistance from Pilar Herrera-Fierro, Vishva Ray, and Sandrine Martin—supported by the National Science Foundation Major Research Instrumentation award under No. DMR-1428226. Y.L, W.J.L and Y.P.S thank the support of the National Key Research and Development Program under contracts 2016YFA0300404 and the National Nature Science Foundation of China under contracts 11674326, 11774351. We thank Lu Li for helpful discussion.

Author contributions

S.H.S., N.S. and R.H. performed HAADF-STEM and in-situ TEM. S.H.S., N.S., R.H., I.E.B. and L.F.K. performed 4D-STEM experiments. S.H.S., S.N., J.G, T.B. and J.T.H. fabricated samples for electronic measurements. S.N., N.V. and J.T.H. performed electronic measurements. X.L. and L.Z. performed RA-SHG measurements. P.D., Z.L measured optical absorption. Y.L, W.J.L and Y.S. grew $1T\text{-TaS}_x\text{Se}_{2-x}$ crystals. S.H.S., R.H. and K.S. provided theoretical interpretation. S.H.S. and R.H. prepared the manuscript. All authors reviewed and edited the manuscript.

Figures

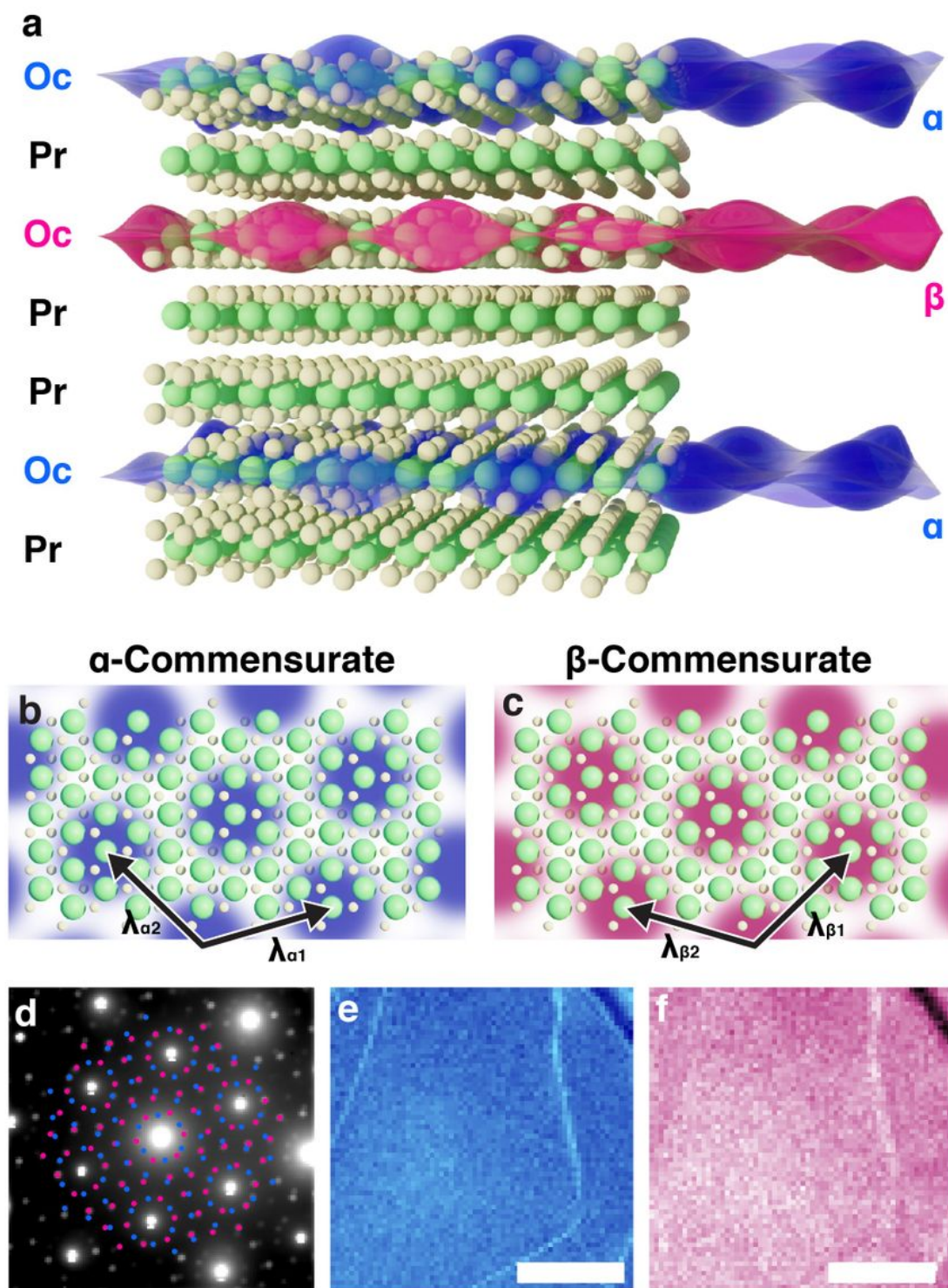


Figure 1

Twinned, commensurate CDW at room temperature in ultrathin TaS₂. a) Schematic illustration of room-temperature, out-of-plane twinned, commensurate CDW in 1T-TaS₂. Blue and red overlays represent CDW twins within octahedrally coordinated TaS₂. Metallic prismatic polytypes isolate octahedral layers to

stabilize tC-CDWs. b, c) Twin superlattice structure illustrated for α and β C-CDW, respectively. d) Average diffraction pattern of twinned, C-CDW state over $(870 \text{ nm})^2$ field-of-view reveals two sets of superlattice peaks (marked with blue and red). e, f) Nanobeam diffraction imaging from each set of superlattice peaks maps the coexistence of both CDW twins—expected for twinning out-of-plane. Scale bar is 300 nm.

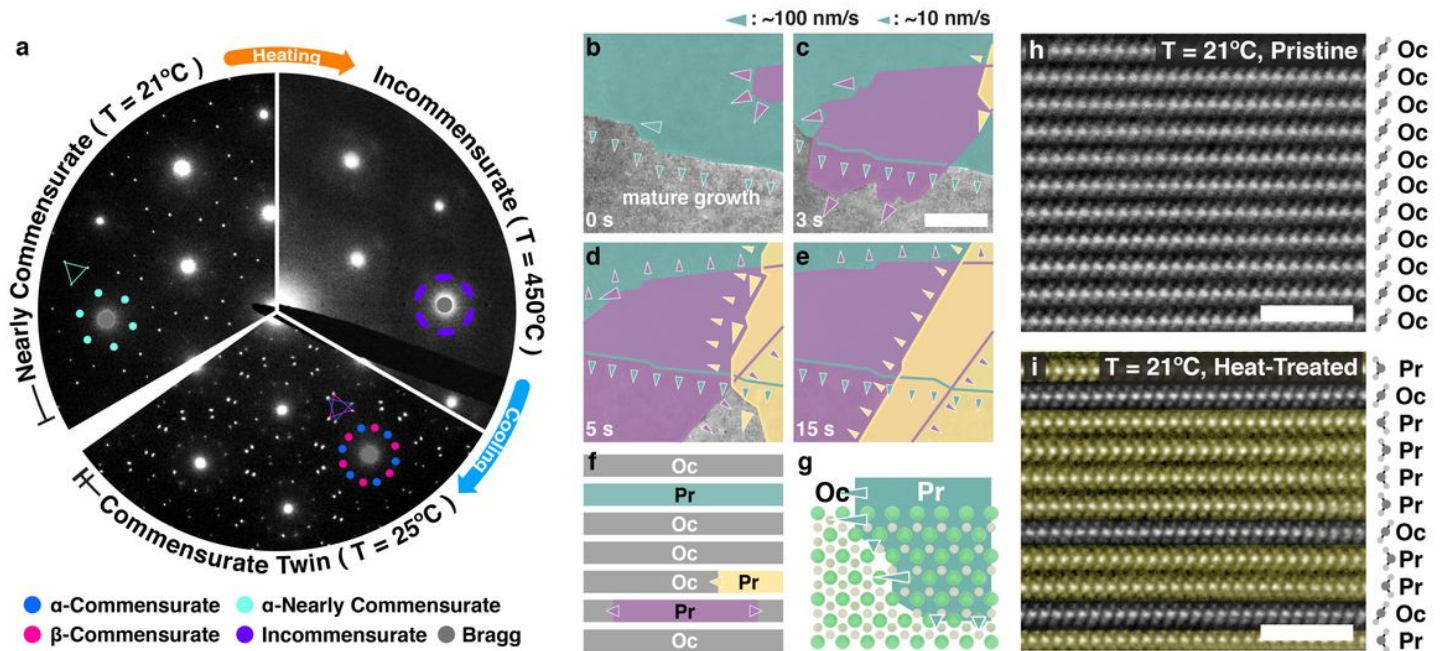


Figure 2

Polytype isolation forms 2D CDW layers. a) Pristine 1T-TaS₂ at room temperature hosts NC-CDW (left). Upon heating the NC phase gives way to IC-CDW (right) at $\approx 350^\circ\text{C}$; the transition is normally reversible. Strikingly, heating above $\approx 450^\circ\text{C}$ then cooling stabilizes tC-CDW (bottom) b–e) In-situ TEM reveals layer-by-layer octahedral to prismatic polytypic transformations during heat treatment. Multiple polytypic domains (denoted green, purple, and yellow) nucleate and grow simultaneously without interaction (See Supplemental Video). Scale bar is 350 nm. f) Schematic cross-section of TaS₂ during layer-by-layer polytypic transition. g) Fast and slow transitions occur along $\approx 1010^\circ$ and $\approx 1120^\circ$ directions respectively. h–i) Atomic resolution crosssectional HAADF-STEM of h) pristine and i) heat-treated TaS_xSe_{2-x} confirms polytypic transformation. After treatment, prismatic (Pr) layers encapsulate monolayers of octahedral (Oc) layers. Scale bar is 2 nm. A selenium doped sample was imaged to enhance chalcogen visibility.

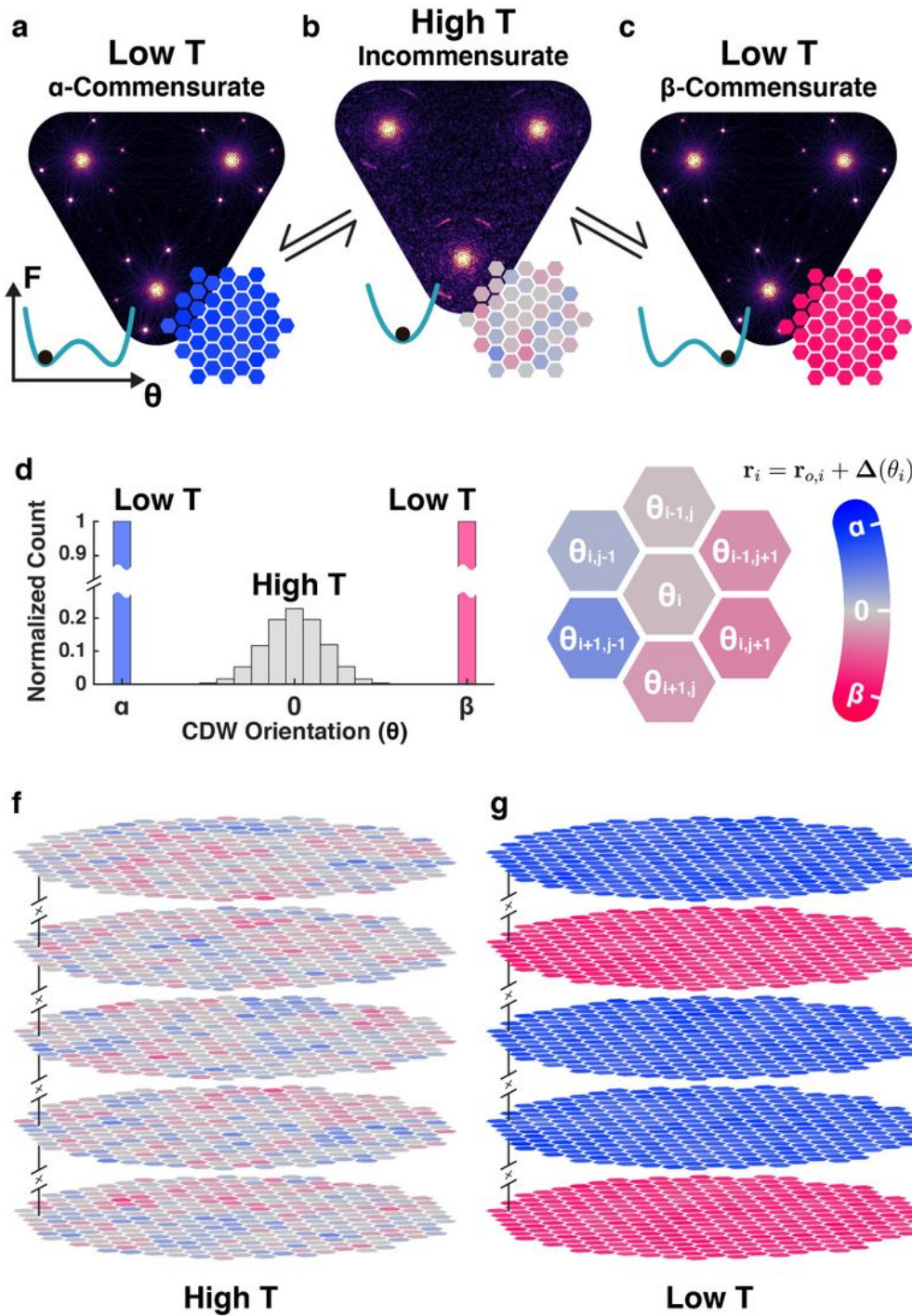


Figure 3

Phenomenological Landau model illustrates formation of commensurate CDWs with out-of-plane twin degeneracy. a–c) The CDW wave-vector direction θ defines an order parameter with degenerate commensurate twins when cooled from IC-CDW phase. Simulated far-field diffraction patterns for a) α -C, b) IC and c) β -C. The free energy (F) landscape (Inset-left) governs the mean θ and the real-space distribution (Insetright). d) Histogram of θ shows zero-centered, wide distribution at high temperature. At

low temperature, the distribution is narrow and centered at $\pm 13.9^\circ$ for either twin. e) Six nearest-neighbor interactions drives longrange order of the CDW. f) At high temperature θ is mean centered and disordered, however, g) at low-temperature each 2D layer converges into either α or β randomly when layers are decoupled.

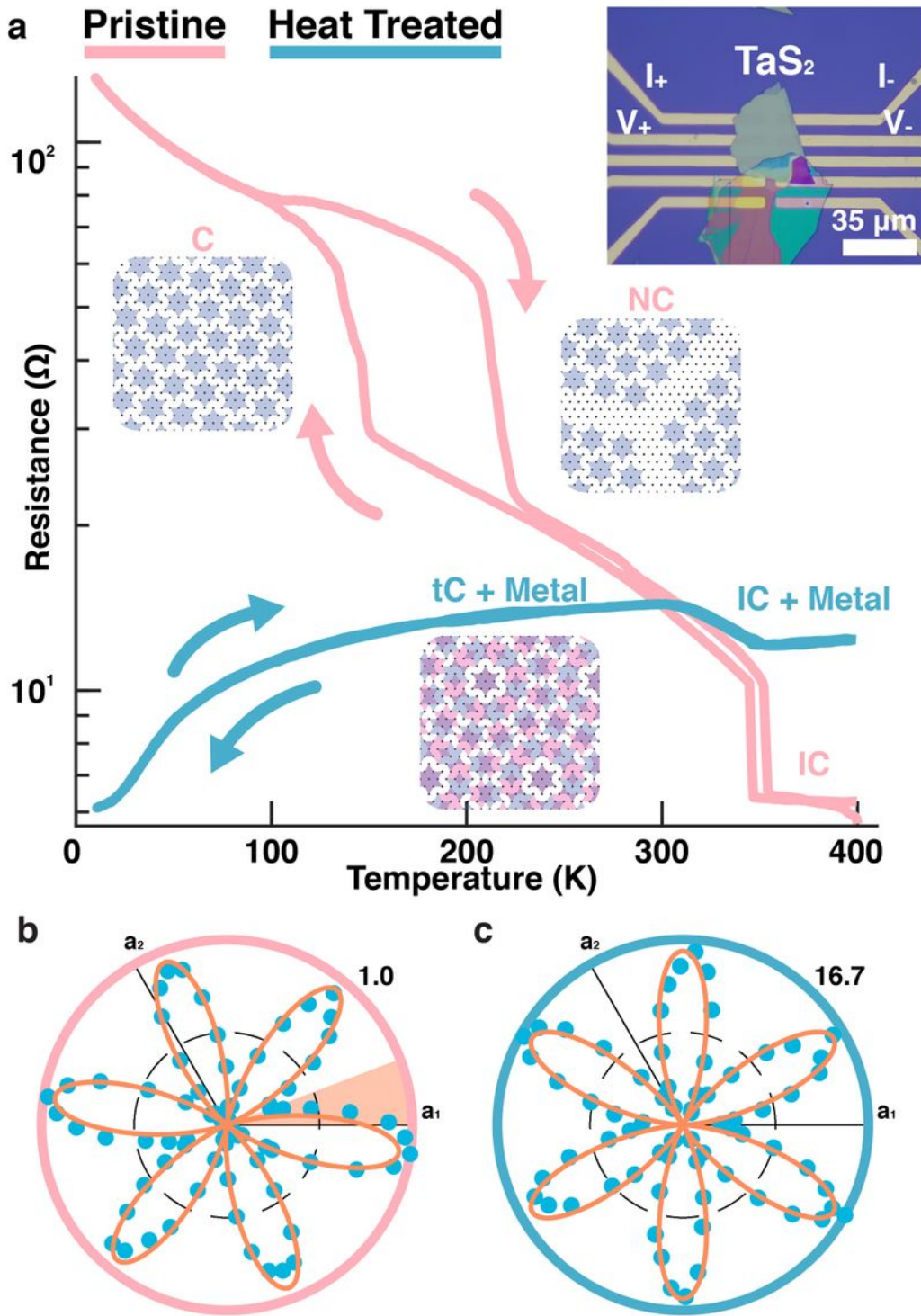


Figure 4

Electronic transport of tC-CDW phase transition and reversibility. a) 4-point in-plane resistance measurement as function of temperature for pristine bulk (pink) and heat-treated (blue) TaS₂. Pristine samples show two jumps in resistance for C₂NC and NC₂IC, whereas the heat treated polytypic heterostructures only feature a single, reversible tC₂IC transition at \approx 350 K corresponding to the enhanced critical temperature for CDW commensuration and disappearance of the NC-CDW. Metallic Prayers dominate the overall trend of the resistance measurement, however, the single jump above room-temperature is a distinct feature of the tC-CDW. Inset) Optical image of the nanofabricated device. b) The RA-SHG pattern for pristine 1T samples display a mismatch between the nominal mirror direction and the crystalline direction, indicating the CDW breaks mirror symmetry. c) After heat treatment, the RA-SHG pattern is symmetric with respect to the crystal, implying equal weights between the α and β states. The SHG intensity also increases with mirror symmetric Pr-layers present.

Supplementary Files

This is a list of supplementary files associated with this preprint. Click to download.

- [SungSIVideo.mov](#)
- [SungSI.pdf](#)